solids

MDPI

Article

Development of SnO_2 Composites as Electron Transport Layer in Unencapsulated $CH_3NH_3PbI_3$ Solar Cells

Gennaro V. Sannino [1,2], Antonella De Maria [1], Vera La Ferrara [1,*], Gabriella Rametta [1], Lucia V. Mercaldo [1], Maria Luisa Addonizio [1], Laura Lancellotti [1], Adriana Pecoraro [3], Ana B. Muñoz-García [3], Michele Pavone [2] and Paola Delli Veneri [1]

[1] Portici Research Center—Italian National Agency for New Technologies, Energy and Sustainable Economic Development (ENEA), Piazzale E. Fermi, 80055 Portici, Italy; gennarovincenzo.sannino@unina.it (G.V.S.); antonella.demaria@enea.it (A.D.M.); gabriella.rametta@enea.it (G.R.); lucia.mercaldo@enea.it (L.V.M.); marialuisa.addonizio@enea.it (M.L.A.); laura.lancellotti@enea.it (L.L.); paola.delliveneri@enea.it (P.D.V.)

[2] Department of Chemical Sciences, Complesso Universitario Monte Sant'Angelo, University of Naples Federico II, Via Cintia 21, 80126 Naples, Italy; michele.pavone@unina.it

[3] Department of Physics "Ettore Pancini", Complesso Universitario Monte Sant'Angelo, University of Naples Federico II, Via Cintia 21, 80126 Naples, Italy; adriana.pecoraro@unina.it (A.P.); anabelen.munozgarcia@unina.it (A.B.M.-G.)

* Correspondence: vera.laferrara@enea.it; Tel.: +39-081-7723322

Abstract: Improving morphological and electronic properties of the electron transport layer (ETL) is a critical issue to fabricate highly efficient perovskite solar cells. Tin dioxide is used as an ETL for its peculiarities such as low-temperature solution-process and high electron mobility and several handlings have been tested to increase its performances. Herein, SnO_2:ZnO and SnO_2:In_2O_3 composites are studied as ETL in planar n-i-p $CH_3NH_3PbI_3$ solar cells fabricated in ambient air, starting from glass/ITO substrates. Morphological, electrical and optical properties of zinc- and indium-oxide nanoparticles (NPs) are investigated. First-principle calculations are also reported and help to further explain the experimental evidences. Photovoltaic performances of full devices show an improvement in efficiency for SnO_2:In_2O_3–based solar cells with respect to pristine SnO_2, probably due to a suppression of interfacial charge recombination between ITO/ETL and ETL/perovskite. Moreover, a better homogeneity of SnO_2:In_2O_3 deposition with respect to SnO_2:ZnO composites, conducts an increase in perovskite grain size and, consequently, the device performances.

Keywords: electron transport layer; tin dioxide; composites; perovskite solar cell; interfaces

Citation: Sannino, G.V.; De Maria, A.; La Ferrara, V.; Rametta, G.; Mercaldo, L.V.; Addonizio, M.L.; Lancellotti, L.; Pecoraro, A.; Muñoz-García, A.B.; Pavone, M.; et al. Development of SnO_2 Composites as Electron Transport Layer in Unencapsulated $CH_3NH_3PbI_3$ Solar Cells. *Solids* **2021**, 2, 407–419. https://doi.org/10.3390/solids2040026

Academic Editor: Philippe Leclère

Received: 30 October 2021
Accepted: 6 December 2021
Published: 16 December 2021

1. Introduction

Perovskite solar cells (PSCs) represent a fast-developing technology and have been attracting enormous interest for the last decade thanks to their high efficiencies and low production costs that are both fundamental requirements for scalability. The recent record of 25.5% [1], established by UNIST, demonstrates the great potential of PSCs.

The PSC is a multi-component device and there are many aspects of the production process that can be addressed in order to promote the scalability. The perovskite is sandwiched between an electron transport layer (ETL) and a hole transport layer (HTL), which extract and transport the photo-generated electrons and the holes in the perovskite to the external circuit, respectively.

In the conventional architecture, namely n-i-p, the ETL and the transparent conductive oxide (TCO), such as indium tin oxide (ITO), form the front electrode providing a good transparency to visible light. The perovskite is deposited on top of the ETL and the full device is completed with a back electrode composed by a metal-coated HTL.

The ETL plays a central role in obtaining PSCs with high performances and sustainable costs. In addition to the electron extraction, this component hinders the hole transfer, thus preventing undesirable charge recombination processes and maximizing the current

generated by the solar cell. Suitable ETL should provide a proper alignment of the valence and conduction bands (VB and CB) with the perovskite ones.

Titanium dioxide has been the most used ETL material, providing so far the best results. However, TiO_2 has several drawbacks. It has a relatively low film electron mobility (~10^{-5} cm^2 V^{-1} s^{-1}) [2] and a high-temperature deposition process (about 500 °C), which increases the energy pay-back time and hinders its use in tandem or flexible solar cells [3]. Moreover, TiO_2-based PSCs degrade rapidly under UV illumination due desorption of oxygen adatoms [4], and such instability limits further applications. Hence, the design of alternative materials to substitute TiO_2 as ETL is a current challenge in the field of PSCs. In this context, tin(IV) oxide (SnO_2) is considered the most promising candidate as ETL. In particular, SnO_2 nanoparticles (NPs) provide good anti-reflective properties and thermal stability [5], and are less hygroscopic [6] and more stable under UV radiation [7] than TiO_2. The latter two properties avoid the degradation of the perovskite layer and ensure the long term stability of the device [8]. Moreover, SnO_2 has a wider bandgap (~3.8 eV [9]), which avoids absorption of high energy photons. Its higher electron mobility (~10^{-3} cm^2 V^{-1} s^{-1} [10]) reduces charges accumulation at the ETL/perovskite interface, improving the electron transport efficiency and decreasing undesired carrier recombination processes [11]. Only a few years ago, several groups achieved good results using SnO_2 as ETL [12–14], but the performances were still much lower than TiO_2-based devices. The reason was attributed to the high temperature (450 °C) used during the annealing that produces a large amount of charge traps and recombination centers in the layer such as oxygen vacancies [15]. To avoid these defects, deposition processes with low temperature have been developed. Jiang et al. [2] used SnO_2 colloidal precursor to procure dense and pinhole-free film. The SnO_2 nanoparticles precursor was spin coated on ITO substrate and post-annealed at 150 °C. Actually, PSCs based on SnO_2 are widely studied in many works [16–19]. The low temperature process suggested the potential of SnO_2 as ETL also in tandem with perovskite-silicon solar cells [20,21]. Several strategies have been adopted to further increase its performance. The addition of dopants [22–24], surface passivation treatments [25,26], and bilayers composed by different ETL materials [27–30] or the use of nanocomposites [31] are typical material handlings used to modify the electronic properties, or improve the ETL/perovskite interfacial contact and the band alignment.

In this paper, we explore the effects of combining tin dioxide with other metal oxides to form composites deposited on two different ITO-based substrates for realizing methylammonium lead triiodide perovskite ($MAPbI_3$) solar cells (device configuration is shown in Figure S1). In particular, we built unencapsulated PSCs with a n-i-p planar structure using SnO_2:In_2O_3 or SnO_2:ZnO composites as ETL. Both ETL and $MAPbI_3$ were spin-coated in ambient air. For $MAPbI_3$ deposition, a "one-step" spinning procedure is used, with opportune anti-solvent, which proved to be one of possible strategies to counteract moisture during the fabrication process [32,33]. Indeed, many studies focus on the manufacturing of perovskite to make the whole process compatible with standard environmental conditions [34–38]. Doped Spiro-OMeTAD [39] was employed as HTL and Au and ITO as back and front electrodes, respectively. Photovoltaic performances, also in this case acquired in air, were compared. We also performed a state-of-the-art density functional theory (DFT) [40,41] study in order to provide a microscopic understanding of the ETL electronic structure.

We found an improvement in fill factor (FF) both for SnO_2:In_2O_3- and SnO_2:ZnO-based devices, leading to an increment in efficiency only if In_2O_3 NPs were used. Both experimental and theoretical results suggest that the introduction of indium oxide nanoparticles can refine the interfacial contact with ITO and perovskite inducing a uniform and pinhole-free perovskite film deposition and enhancing the electron transfer. SnO_2:In_2O_3 composites, deposited as ETL in PSCs without control of environmental conditions, allow to reach satisfactory efficiencies.

2. Experimental Section

2.1. Materials

Indium oxide (In_2O_3) nanopowder, zinc oxide (ZnO) nanopowder, lead iodide (PbI_2) (99.999%), spiro-OMeTAD, 4-tert-butylpyridine (*t*-BPY), FK 209 Co(III) TFSI salt, dimethyl formamide (DMF), dimethyl sulfoxide (DMSO), lithium-bis(tri-fluoromethylsulfonyl)-imide (Li-TFSI), diethyl ether, acetonitrile (ACN) and chlorobenzene (CBZ) were purchased from Sigma-Aldrich/Merck, St. Louis, MO, USA. The tin(IV) oxide 15% *w*/*w* in H_2O colloidal dispersion was obtained from Alfa-Aesar, by Thermo Fisher GmbH, Kandel, Germany. Methylammonium iodide (MAI) was prepared following the procedure in the reference [42]. An excess of methylamine (50 mL) was reacted with hydroiodic acid (20 mL) in 200 mL of ethanol under N_2 atmosphere at room temperature for 2 h. Crystallization of MAI was achieved using a rotary evaporator. Methylamine (33 wt% in absolute ethanol) and hydroiodic acid (57 wt% in water) were purchased from ACROS Organics, Geel, Belgium.

2.2. Device Fabrication and Characterization

We built PSCs with the following layout ITO/ETL/$MAPbI_3$/doped-Spiro-OMeTAD/Au using SnO_2:ZnO or SnO_2:In_2O_3 composites as ETL and compare their performances with the SnO_2–based device. Two different ITO glass substrates were used: the former was purchased by Kintec (named comITO) and the latter was fabricated in our laboratories (named labITO) using a RF magnetron sputtering system MRC-643 equipped with a loadlock. Sputtering processes were carried out by using an ITO ceramic target (10 wt% SnO_2) in argon atmosphere at RF-power of 400 W. ITO films were deposited on non-intentionally heated Corning Eagle XG glass substrate. All the ITO substrates were treated under UV-ozone for 30 min before the ETL film deposition to enhance the substrate wettability. Three ETL solutions were prepared in air starting from diluting an equal volume of Alfa-Aesar SnO_2 colloidal dispersion with deionized water (SnO_2:H_2O = 1:1), or 1.5% *w*/*w* dispersions of In_2O_3 or ZnO NPs in deionized water (SnO_2:In_2O_3 = 1:1 and SnO_2:ZnO = 1:1). The ETL solutions were centrifuged and supernatant was spin-coated in air at 6000 rpm for 50 s and the substrates were dried on a hot plate at 150 °C for 30 min. $MAPbI_3$ layer was obtained with the "one-step" solvent engineering approach [43,44]. The $MAPbI_3$ precursor solution (1.4 M) was obtained in a N_2-filled glove box by dissolving PbI_2 and MAI in a mixture of DMF:DMSO (9:1, volume ratio). ETL-based substrates were treated again under 7 min of UV-ozone. Finally, the precursor solution was spin-coated onto substrates in air at 1000 rpm (200 rpm/s) for 10 s and then at 5000 rpm (1000 rpm/s) for 45 s, dripping the diethyl ether anti-solvent in the proper time during the second step spinning. Then, the substrates were dried on a hot plate beforehand at 50 °C for 2 min and after at 100 °C for 10 min. Environmental conditions were monitored (45–70% of relative humidity and 20–25 °C). A 0.060 M solution of Spiro-OMeTAD, as HTL, was prepared in a N_2-filled glove box dissolving the Spiro-OMeTAD powder in CBZ. After, considering 1 mL of solution, it was sequentially doped as in the reference [39] with 28 µL of t-BPY, 17 µL of the lithium solution (1.8 M Li-TFSI in ACN), and 7.5 µL of the cobalt solution (4.0 M FK 209 Co(III) TFSI salt in ACN) few hours before the HTL spin coating deposition. Finally, the doped Spiro-OMeTAD solution was spin-coated in a N_2-filled glove box at 4000 rpm for 30 s and 80 nm gold electrodes were deposited using a thermal evaporator (by Morfield).

Scanning electron microsopy (SEM) images were collected by Thermo Fisher Scientific Phenom pro X SEM. Dynamic light scattering (DLS) measurements were performed with a Zetasizer Nano ZS He-Ne laser 633 nm, 4 mW. Steady-state photoluminescence (PL) was measured with a Renishaw Raman inVia Re-flex system with excitation at 514 nm by an Argon ion laser. Transmission spectra were measured using the PerkinElmer λ-900 spectrophotometer. KLA-Tencor P7 profilometer was used to measure the thickness of the ETLs. Work functions of two different ITO substrates were carried on through Kelvin Probe Technique using an SKP5050 Scanning Kelvin Probe (KP Technology, Wick, Caithness, Scotland). Solar cells were characterized under the AM1.5G spectrum generated by a class

AAA dual-lamp solar simulator (WACOM Electric Co. LTD, Tanaka, Fukaya-shi, Saitama) in uncontrolled moisture and temperature conditions. The current–voltage characteristics of the devices were obtained by applying external voltage while recording the generated photocurrent using a Keithley (Model 2651A) high power system source meter. JV data acquisition was performed with scan rate of 2 V/s for all the electrical measurements and the scan range was 1.2 V to −0.1 V (reverse scan direction). The irradiated area was 0.11 cm^2, defined by applying a shadow mask. JV characteristics were recorded immediately after the gold electrode evaporation.

2.3. First-Principle Calculations

We performed periodic spin-polarized DFT calculations with the GGA/PBE density functional [45,46] and plane wave basis set with the Vienna Ab-initio Simulation Package program (VASP, version 5.4.1) [47–50]. We computed the CB energy position of all the investigated ETL materials following the approach proposed by Toroker et al. [51]. We compared the results with the CB edge of the $MAPbI_3$ perovskite (−4.13 eV) that has been calculated at the same level of theory [52]. The ionic cores were represented with projector-augmented wave (PAW) potentials [53,54] and, in particular, $2s^2 2p^4$ electrons for O, $5s^2 5p^2$ electrons for Sn, $3d^{10} 4p^2$ electrons for Zn, and $5s^2 5p^1$ electrons for In were treated as valence electrons. The long-range interactions were taken into account and treated with Grimme's DFT-D3(BJ) correction method [55–57]. The break condition of the SC-loop was set to 10^{-5} eV. All atoms were allowed to relax freely to equilibrium in bulks and slab models until the force on each of them was less than 0.03 eV/Å. Bulk structure optimizations were performed considering the most thermodynamically stable phase of each metal oxide. These are the rutile structure (space group $P4_2/mnm$) for SnO_2, the bixbyte structure (space group $Ia\bar{3}$) for In_2O_3 and the wurtzite structure (space group $P6_3mc$) for ZnO. Surface slab models were constructed starting from PBE-D3BJ optimized bulk geometries. The surfaces considered in our study are the most stable non-polar surfaces, i.e., the (110) surface for SnO_2 [58], the (111) surface for In_2O_3 [59] and the $(10\bar{1}0)$ surface for ZnO [60]. Slabs dimensions are chosen to reach an accurate description of the bulk properties in the inner layers. Thus, we built 5-layer slab models of SnO_2 (110) and ZnO $(10\bar{1}0)$ containing 30 and 20 atoms, respectively, and a 2-layer slab (160 atoms) for In_2O_3 (111). In all the models, a 10 Å vacuum slab was inserted. Plane waves energy cut-off has been set to 800 eV in all calculations. Γ-centered Monkhorst-Pack k-point meshes were used for SnO_2 (6 × 6 × 9), ZnO (8 × 8 × 4) and In_2O_3 (4 × 4 × 4) bulks, and these have been scaled accordingly in surface models. Experimental band gaps were used in the approach implemented to calculate CB edges [51] (SnO_2 = 3.6 eV [61]; In_2O_3 = 3.7 eV [62]; ZnO = 3.2 eV [63]).

3. Results and Discussion

We carried out experimental characterizations in order to understand the effect of nanoparticles on the solar cell parameters. DLS measurements were performed on the ETL precursor solutions and different NPs size distribution patterns were obtained (Figure 1). The solution with In_2O_3 NPs shows a unique predominant population at ~100 nm. Such a narrow distribution of hydrodynamic radii is expected to generate smooth, compact and homogeneous ETLs.

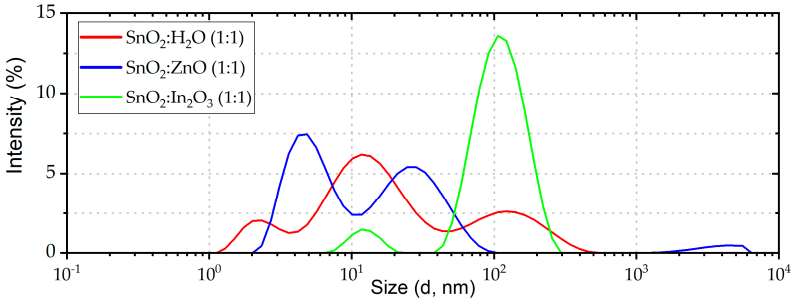

Figure 1. Size distributions of the ETL precursor solutions NPs obtained from DLS measurements.

In SnO_2:ZnO solution, the highest peak is at ~5 nm, highlighting a predominant NPs population with smaller dimensions than the solution containing only SnO_2 NPs. Composites and SnO_2 precursor solutions were deposited on ITO as described in experimental section. This procedure provides layers with almost the same thickness (~30 nm) for all the ETLs. SEM images of the perovskite layer were acquired on each ETL (Figure 2). When $MAPbI_3$ is deposited on SnO_2:In_2O_3 we observe larger perovskite grains with respect to the SnO_2:ZnO composite. This is ascribed to uniform distribution of NPs into SnO_2:In_2O_3, which improves the perovskite crystal growth, generating large grains. Instead, small aggregates of SnO_2:ZnO composite generate pinholes onto ITO substrates and form rougher surfaces that increase the density of nucleation sites for the perovskite crystal growth [64]. In Table S1 and Figure S2 data and images of grain analysis are shown. These results are in agreement with the observations deduced with DLS measurements.

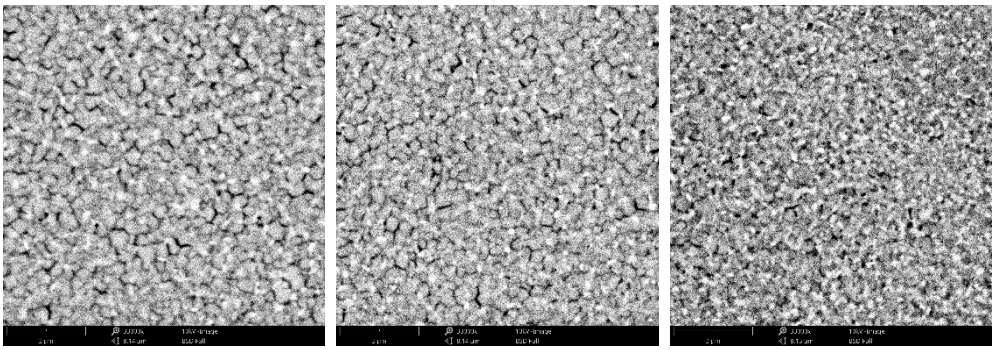

(**a**) (**b**) (**c**)

Figure 2. SEM images of $MAPbI_3$ perovskite deposited on SnO_2 ETL (**a**), SnO_2:In_2O_3 composite ETL (**b**) and SnO_2:ZnO composite ETL (**c**); white bars indicate a length of 2 μm.

Transmission UV-Vis spectra (Figure S3) reveal that both indium and zinc oxide NPs do not affect the optical transparency and anti-reflective properties of the tin dioxide/ITO unit. Transparency is about 80% in the visible spectrum, increasing up to 90% in the range 550–600 nm. The band gap extracted from Tauc plot is ~3.8 eV (inset of Figure S3), in agreement with other works [65–67].

We performed steady-state PL measurements on solar cell precursors without HTL, i.e., nominally identical $MAPbI_3$ films deposited on ITO/SnO_2, ITO/SnO_2:ZnO, ITO/SnO_2:In_2O_3 and ITO alone for comparison, in order to test the proposed ETLs for their ability to maintain a high photoluminescence [68]. A reduction in PL intensity is indicative of enhanced non-radiative recombination and thus reduced quasi-Fermi level splitting. Therefore, luminescence should be maximized to avoid V_{OC} losses. The measured PL spectra are shown in Figure 3. No major PL quenching is found. Similar emission is observed for all the samples, with peak intensity by only a factor ~2 lower than the reference ITO/$MAPbI_3$ stack. This suggests only slightly increased non-radiative recombination vs. the reference stack (which could be at the ETL/$MAPbI_3$ interface and/or in the $MAPbI_3$ film itself when

deposited on the ETLs vs. ITO). In addition, the tested ETLs should, in principle, all allow for similar V_{OC}.

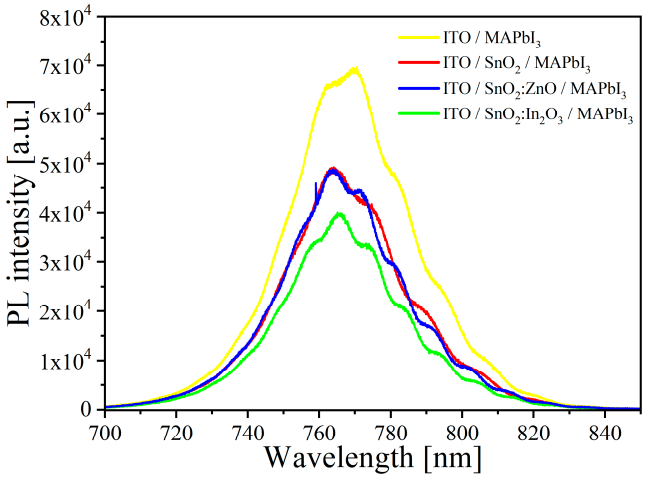

Figure 3. Photoluminescence spectra of $MAPbI_3$ perovskite deposited on different layers.

Full devices, starting from commercial ITO (comITO) substrates, were fabricated, introducing these composites as ETL and compared with SnO_2 layer. All the devices with SnO_2 or SnO_2:In_2O_3 as ETL were working, whilst some SnO_2:ZnO-based devices did not work. In Figure 4 box plot charts of normal distribution of PSCs are reported for all PV parameters. Short circuit current density decreases in solar cells with ZnO NPs inserted in the SnO_2 ETL, probably due to growth of smaller perovskite grains (Figure 2c) with more grain boundaries, which act as recombination centers. Conversely, no drop in V_{OC} is recorded, as expected by PL spectra. Generally, this parameter is less dependent on the undesired recombination processes at interfaces, with respect to Jsc.

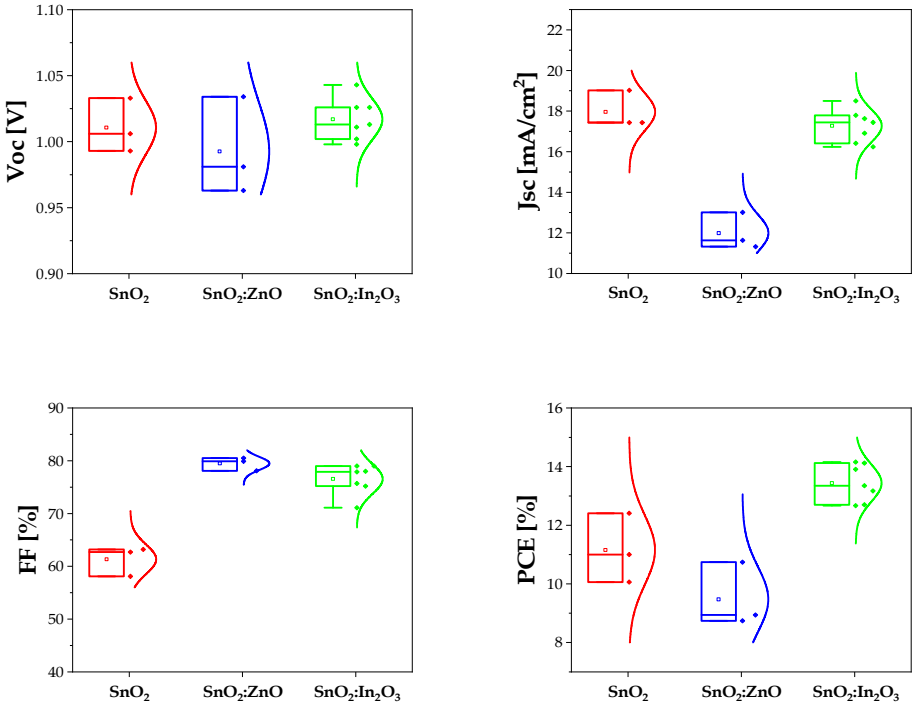

Figure 4. PV parameters of SnO_2 (in red), SnO_2:ZnO (in blue) and SnO_2:In_2O_3 (in green) as different ETL for perovskite solar cells.

We note that Jsc and V_{OC} for tin dioxide and SnO_2:In_2O_3 composite-based PSCs are quite similar, whereas the FF is lower for the reference. Ideally, FF depends on V_{OC} [69], but in the real devices many losses are present. This parameter improves when composites are used, probably due to higher electron mobility and transport ability of SnO_2:In_2O_3 or SnO_2:ZnO ETL leading to improved charge transport balance and the reduction in the interface charge accumulation [70,71]. Furthermore, the homogeneous population of the SnO_2:In_2O_3 precursor solution ensures a better interfacial contact of ITO and the perovskite with the composite film, which further enhances the charge transport. In Table 1 average data and standard deviation of PSCs photovoltaic parameters, realized starting from commercial ITO substrates, are reported. The enhancement was confirmed by the fabrication of different batches (in Figures S4 and S5 and Table S2, JV data and EQE measurements extracted from another batch are reported as evidence).

Table 1. Average data and standard deviation from J-V measurements of SnO_2, SnO_2:ZnO and SnO_2:In_2O_3-based PSCs starting from comITO substrates.

ETL	Jsc [mA/cm^2]	V_{OC} [V]	FF [%]	PCE [%]
SnO_2	18 ± 1	1.01 ± 0.02	61 ± 3	11.2 ± 1.2
SnO_2:ZnO	12 ± 1	0.99 ± 0.04	79 ± 1	9.5 ± 1.1
SnO_2:In_2O_3	17 ± 1	1.02 ± 0.02	73 ± 3	13.4 ± 0.6

This effect is also evident if we use ITO fabricated in our laboratories (labITO). Results are reported in Figure 5 and in Table 2, where J-V and PV parameters of devices are shown, respectively.

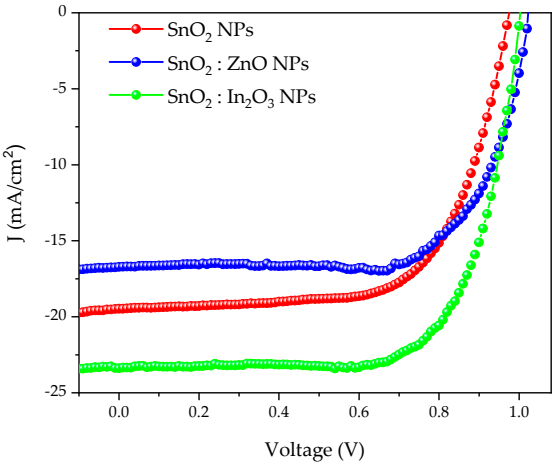

Figure 5. J-V curves of SnO_2 (in red), SnO_2:ZnO (in blue) and SnO_2:In_2O_3 (in green), starting from labITO.

Table 2. Photovoltaic parameters of devices with different ETLs starting on labITO.

ETL	Jsc [mA/cm^2]	V_{OC} [V]	FF [%]	PCE [%]
SnO_2	19.5	0.98	65.8	12.5
SnO_2:ZnO	16.7	1.02	70.2	12.0
SnO_2:In_2O_3	23.3	1.00	70.3	16.4

We note an enhancement of performances caused by higher Jsc values. Then, we characterized labITO and comITO substrates. Transmittance and absorbance spectra are reported in Figure 6 and main optical parameters Eg and A_{av} (specifically, band gap and average optical absorbance weighted on the solar spectrum between 350 and 800 nm), sheet resistance, resistivity and charge carrier concentrations are shown in Table 3. In Figure 6 it

is evident that the commercial TCO presents a higher free carrier absorption in the red-NIR spectral region, due to a doping level two times higher than ITO film produced in our laboratory, as evident in Table 3. The higher Eg value observed for comITO with respect to labITO can be predominantly attributed to a higher charge carrier concentration, according to the Burstein–Moss effect for n-type degenerate semiconductors. This is the reason for the observed blue shift of the absorption edge. However, ITO films have a quite similar average optical absorbance value. Furthermore, another analysis was 2D work function maps, acquired over an area 5 × 10 mm^2 (shown in Figure 7), indicating mean absolute values of 4.82 eV and 4.62 eV for labITO and comITO, respectively. These values highlight that ITO involves different interfacial behavior when it is used as substrate. Then, the enhancement of Jsc parameter could be due to combined effects between lower charge carrier concentration and a better interfacial contact of ITO/ETL when labITO is used. It is also important to evidence that if SnO_2:In_2O_3 is used as ETL, electrical characteristics recorded immediately after full device fabrication are improved with respect to PSCs based on pristine SnO_2 which instead require a storage time to increase its PV performance [72,73].

Spin-polarized DFT calculations were also performed to gain insight on the CB positions of the materials under investigation. The proper alignment between the CB edges of the ETL and the absorber material is critical for a proper solar cell operation. The CB edge of the perovskite should lie at a higher energy than the ETL one in order to ensure the electron transfer between the two materials. Their energy difference represents a first estimation of the efficiency of the electron injection process. The obtained results elucidated that tin dioxide CB plays the major role in settling the V_{OC} of the solar cell also when combined with other oxides. In fact, as shown in Figure 8, the CB edge position of the ZnO and In_2O_3 compounds lies higher in energy than SnO_2 CB. Thus, SnO_2 CB position defines in both composites the V_{OC} of the device.

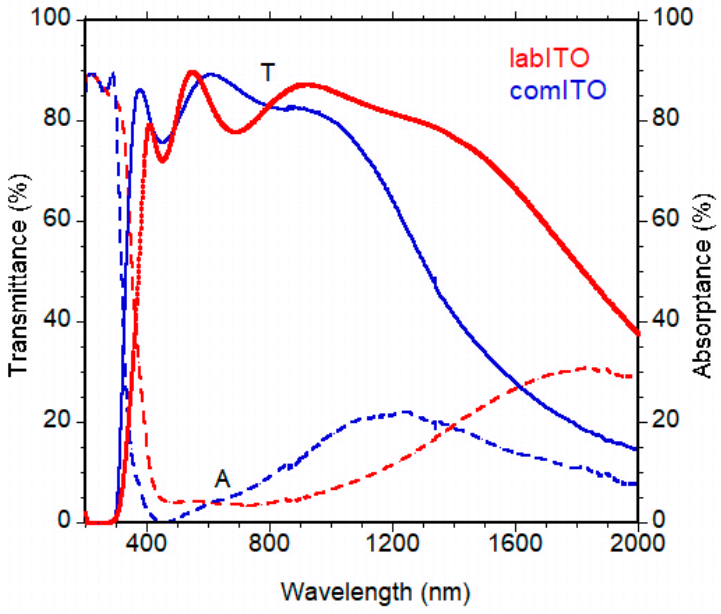

Figure 6. Transmittance and absorptance spectra of comITO and labITO films.

Table 3. Thickness, optical and electrical parameters of comITO and labITO.

TCO	Thickness [nm]	R_{sh} [ohm/sq]	ρ [Ω∗cm] × 10^{-4}	N_e [cm^{-3}] × 10^{21}	A_{av} [%]	E_g [eV]
comITO	180	10	1.8	1.2	8	3.83
labITO	285	11	3.2	0.55	9	3.65

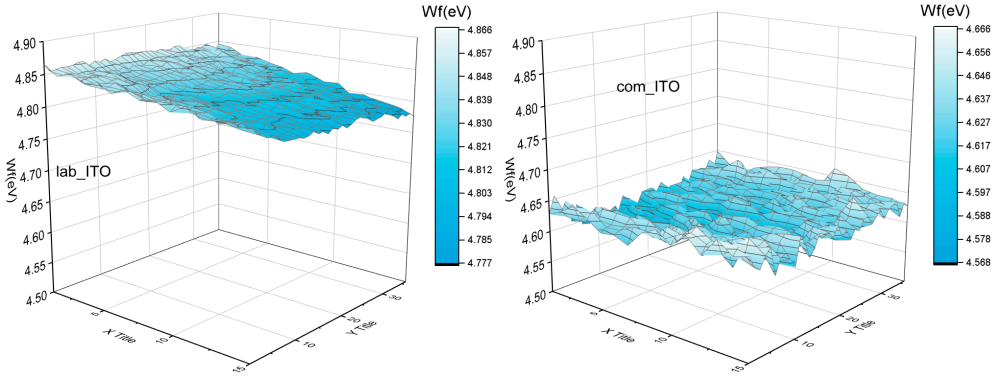

Figure 7. 2D work function maps for labITO and comITO.

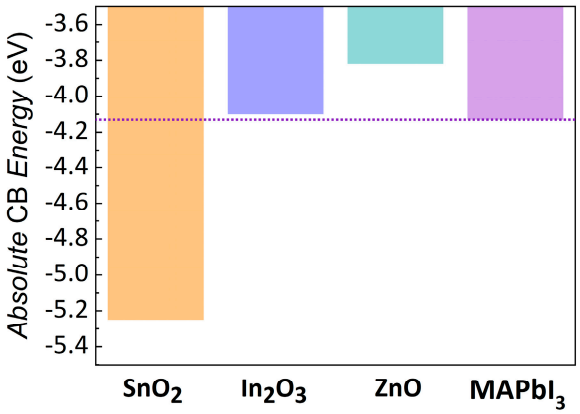

Figure 8. Absolute position of the CB edges extracted from calculations on slab models and compared with $MAPbI_3$ CB edge calculated at the same level of theory [52]; purple line denotes the CB edge of the $MAPbI_3$.

4. Conclusions

In this study, $CH_3NH_3PbI_3$ solar cells have been fabricated in ambient air for testing the performances of the SnO_2:In_2O_3 and SnO_2:ZnO composites as ETL. Insertion of In_2O_3 NPs inside the SnO_2 solution effectively improved the device performances. In particular, a higher efficiency has been independently measured from starting ITO substrates. The enhancement could be due to a better interfacial contact of ITO and perovskite with SnO_2:In_2O_3. Moreover, we addressed this behavior to the distribution of homogenous aggregates in precursor solution, refining the interface with the perovskite and making it more uniform with respect to ZnO NPs, which promotes the growth of small perovskite grains, which are detrimental for PSCs performances. Composites have provided quite the same V_{OC} value of the SnO_2-based device, confirming PL and theoretical results that suggest the SnO_2 CB also in composites define the driving force of the electron transfer process. Therefore, improvements and worsening obtained using composites depend essentially on NPs size distribution, which influences the uniformity and interfacial ETL/perovskite. Our work points out the importance of morphological effects caused by use of composites and benefits offered by ETL precursor solutions with a homogeneous population in order to obtain a high quality of interfaces. In future, different characterization techniques (such as dark J-V) are planned to be used to deeply explore the observed phenomena. Further computational studies are needed to understand at atomic level how the indium- and zinc-oxide structures influence the quality of the interface. At the same time, the investigation of different SnO_2:In_2O_3 ratio in ETL precursor solutions could lead to further improvements of the interfacial contact with the perovskite, so to enhance the electron transfer process.

Supplementary Materials: The following are available online at https://www.mdpi.com/article/10.3390/solids2040026/s1, Figure S1: PSC with n-i-p configuration adopted for our devices; Figure S2: Grain size analysis of $MAPbI_3$ crystals growth on SnO_2 (a), SnO_2:In_2O_3 (b) and SnO_2:ZnO (c) ETLs. Data are shown in Table S1; Figure S3: UV-vis transmission spectra of ETLs on ITO coated glass substrates and Tauc's plot (inset); Figure S4: PV parameters of SnO_2 (in red) and SnO_2:In_2O_3 (in green) as different ETL for perovskite solar cells. Data are shown in Table S2; Figure S5: EQE spectra for SnO_2 (in red) and SnO_2:In_2O_3 (in green) based PSCs; Table S1: Average value of perovskite grain sizes weighted by count; Table S2: Average data and standard deviation extracted from J-V measurements of SnO_2 and SnO_2:In_2O_3-based PSCs.

Author Contributions: Conceptualization, G.V.S., A.D.M., V.L.F. and G.R.; Formal analysis, A.P.; Investigation, G.V.S., L.V.M., M.L.A. and L.L.; Project administration, P.D.V.; Supervision, A.D.M., V.L.F., A.B.M.-G., M.P. and P.D.V.; Validation, A.D.M., V.L.F., G.R. and A.B.M.-G.; Writing—original draft, G.V.S.; Writing—review and editing, G.V.S., A.D.M., V.L.F., G.R., L.V.M., M.L.A., L.L., A.P., A.B.M.-G., M.P. and P.D.V. All authors have read and agreed to the published version of the manuscript.

Funding: This work was supported by the Italian Ministry of Ecological Transition in the frame-work of the Operating Agreement with ENEA for Research on the Electric System.

Institutional Review Board Statement: Not applicable.

Informed Consent Statement: Not applicable.

Data Availability Statement: Not applicable.

Acknowledgments: The computing resources and the related technical support used for this work have been provided by the CRESCO/ENEAGRID High Performance Computing infrastructure and its staff [F. Iannone et al.]. The CRESCO/ENEAGRID High Performance Computing infrastructure is funded by ENEA, the Italian National Agency for New Technologies, Energy and Sustainable Economic Development and by Italian and European research programmes (see http://www.cresco.enea.it/english for information 30 October 2021).

Conflicts of Interest: The authors declare no conflict of interest.

References

1. NREL Best Research-Cell Efficiencies. Available online: https://www.nrel.gov/pv/assets/pdfs/best-research-cell-efficiencies.20200104.pdf (accessed on 13 February 2021).
2. Jiang, Q.; Zhang, L.; Wang, H.; Yang, X.; Meng, J.; Liu, H.; Yin, Z.; Wu, J.; Zhang, X.; You, J. Enhanced electron extraction using SnO_2 for high-efficiency planar-structure $HC(NH_2)_2PbI_3$-based perovskite solar cells. *Nat. Energy* **2016**, *2*, 16177. [CrossRef]
3. Green, M.A.; Ho-Baillie, A.; Snaith, H.J. The emergence of perovskite solar cells. *Nat. Photonics* **2014**, *8*, 506–514. [CrossRef]
4. Leijtens, T.; Eperon, G.E.; Pathak, S.; Abate, A.; Lee, M.M.; Snaith, H.J. Overcoming ultraviolet light instability of sensitized TiO_2 with meso-superstructured organometal tri-halide perovskite solar cells. *Nat. Commun.* **2013**, *4*, 2885. [CrossRef]
5. Noh, M.F.M.; Soh, M.F.; Teh, C.H.; Lim, E.L.; Yap, C.C.; Ibrahim, M.A.; Ludin, N.A.; Teridi, M.A.M. Effect of temperature on the properties of SnO_2 layer fabricated via AACVD and its application in photoelectrochemical cells and organic photovoltaic devices. *Sol. Energy* **2017**, *158*, 474–482. [CrossRef]
6. Song, J.; Zheng, E.; Bian, J.; Wang, X.F.; Tian, W.; Sanehira, Y.; Miyasaka, T. Low-temperature SnO_2-based electron selective contact for efficient and stable perovskite solar cells. *J. Mater. Chem. A* **2015**, *3*, 10837–10844. [CrossRef]
7. Tiwana, P.; Docampo, P.; Johnston, M.B.; Snaith, H.J.; Herz, L.M. Electron Mobility and Injection Dynamics in Mesoporous ZnO, SnO_2, and TiO_2 Films Used in Dye-Sensitized Solar Cells. *ACS Nano* **2011**, *5*, 5158–5166. [CrossRef]
8. Wang, C.; Zhao, D.; Grice, C.R.; Liao, W.; Yu, Y.; Cimaroli, A.; Shrestha, N.; Roland, P.J.; Chen, J.; Yu, Z.; et al. Low-temperature plasma-enhanced atomic layer deposition of tin oxide electron selective layers for highly efficient planar perovskite solar cells. *J. Mater. Chem. A* **2016**, *4*, 12080–12087. [CrossRef]
9. Xiong, L.; Guo, Y.; Wen, J.; Liu, H.; Yang, G.; Qin, P.; Fang, G. Review on the Application of SnO_2 in Perovskite Solar Cells. *Adv. Funct. Mater.* **2018**, *28*, 1802757. [CrossRef]
10. Xu, Z.; Teo, S.H.; Gao, L.; Guo, Z.; Kamata, Y.; Hayase, S.; Ma, T. La-doped SnO_2 as ETL for efficient planar-structure hybrid perovskite solar cells. *Org. Electron.* **2019**, *73*, 62–68. [CrossRef]
11. Fakharuddin, A.; Schmidt-Mende, L.; Garcia-Belmonte, G.; Jose, R.; Mora-Sero, I. Interfaces in Perovskite Solar Cells. *Adv. Energy Mater.* **2017**, *7*, 1700623. [CrossRef]
12. Li, Y.; Zhu, J.; Huang, Y.; Liu, F.; Lv, M.; Chen, S.; Hu, L.; Tang, J.; Yao, J.; Dai, S. Mesoporous SnO_2 nanoparticle films as electron-transporting material in perovskite solar cells. *RSC Adv.* **2015**, *5*, 28424–28429. [CrossRef]
13. Dong, Q.; Shi, Y.; Wang, K.; Li, Y.; Wang, S.; Zhang, H.; Xing, Y.; Du, Y.; Bai, X.; Ma, T. Insight into Perovskite Solar Cells Based on SnO_2 Compact Electron-Selective Layer. *J. Phys. Chem. C* **2015**, *119*, 10212–10217. [CrossRef]

14. Rao, H.S.; Chen, B.X.; Li, W.G.; Xu, Y.F.; Chen, H.Y.; Kuang, D.B.; Su, C.Y. Improving the Extraction of Photogenerated Electrons with SnO_2 Nanocolloids for Efficient Planar Perovskite Solar Cells. *Adv. Funct. Mater.* **2015**, *25*, 7200–7207. [CrossRef]
15. Jiang, Q.; Zhang, X.; You, J. SnO_2: A Wonderful Electron Transport Layer for Perovskite Solar Cells. *Small* **2018**, *14*, 1801154. [CrossRef]
16. Spalla, M.; Planes, E.; Perrin, L.; Matheron, M.; Berson, S.; Flandin, L. Alternative Electron Transport Layer Based on Al-Doped ZnO and SnO_2 for Perovskite Solar Cells: Impact on Microstructure and Stability. *ACS Appl. Energy Mater.* **2019**, *2*, 7183–7195. [CrossRef]
17. Yoo, J.J.; Seo, G.; Chua, M.R.; Park, T.G.; Lu, Y.; Rotermund, F.; Kim, Y.K.; Moon, C.S.; Jeon, N.J.; Correa-Baena, J.-P.; et al. Efficient perovskite solar cells via improved carrier management. *Nature* **2021**, *590*, 587–593. [CrossRef]
18. Zhu, P.; Gu, S.; Luo, X.; Gao, Y.; Li, S.; Zhu, J.; Tan, H. Simultaneous Contact and Grain-Boundary Passivation in Planar Perovskite Solar Cells Using SnO_2-KCl Composite Electron Transport Layer. *Adv. Energy Mater.* **2020**, *10*, 1903083. [CrossRef]
19. You, S.; Zeng, H.; Ku, Z.; Wang, X.; Wang, Z.; Rong, Y.; Zhao, Y.; Zheng, X.; Luo, L.; Li, L.; et al. Multifunctional Polymer-Regulated SnO_2 Nanocrystals Enhance Interface Contact for Efficient and Stable Planar Perovskite Solar Cells. *Adv. Mater.* **2020**, *32*, 2003990. [CrossRef]
20. Albrecht, S.; Saliba, M.; Baena, J.P.C.; Lang, F.; Kegelmann, L.; Mews, M.; Steier, L.; Abate, A.; Rappich, J.; Korte, L.; et al. Monolithic perovskite/silicon-heterojunction tandem solar cells processed at low temperature. *Energy Environ. Sci.* **2016**, *9*, 81–88. [CrossRef]
21. Al-Ashouri, A.; Köhnen, E.; Li, B.; Magomedov, A.; Hempel, H.; Caprioglio, P.; Márquez, J.A.; Vilches, A.B.M.; Kasparavicius, E.; Smith, J.A.; et al. Monolithic perovskite/silicon tandem solar cell with >29% efficiency by enhanced hole extraction. *Science* **2020**, *370*, 1300–1309. [CrossRef] [PubMed]
22. Park, M.; Kim, J.Y.; Son, H.J.; Lee, C.H.; Jang, S.S.; Ko, M.J. Low-temperature solution-processed Li-doped SnO_2 as an effective electron transporting layer for high-performance flexible and wearable perovskite solar cells. *Nano Energy* **2016**, *26*, 208–215. [CrossRef]
23. Halvani Anaraki, E.; Kermanpur, A.; Mayer, M.T.; Steier, L.; Ahmed, T.; Turren-Cruz, S.-H.; Seo, J.; Luo, J.; Zakeeruddin, S.M.; Tress, W.R.; et al. Low-Temperature Nb-Doped SnO_2 Electron-Selective Contact Yields over 20% Efficiency in Planar Perovskite Solar Cells. *ACS Energy Lett.* **2018**, *3*, 773–778. [CrossRef]
24. Akin, S. Hysteresis-Free Planar Perovskite Solar Cells with a Breakthrough Efficiency of 22% and Superior Operational Stability over 2000 h. *ACS Appl. Mater. Interfaces* **2019**, *11*, 39998–40005. [CrossRef]
25. Wang, J.; Datta, K.; Weijtens, C.H.; Wienk, M.M.; Janssen, R.A. Insights into Fullerene Passivation of SnO_2 Electron Transport Layers in Perovskite Solar Cells. *Adv. Funct. Mater.* **2019**, *29*, 1905883. [CrossRef]
26. Tsarev, S.; Dubinina, T.S.; Luchkin, S.Y.; Zhidkov, I.S.; Kurmaev, E.Z.; Stevenson, K.J.; Troshin, P.A. Phenyl-C61-butyric Acid as an Interface Passivation Layer for Highly Efficient and Stable Perovskite Solar Cells. *J. Phys. Chem. C* **2020**, *124*, 1872–1877. [CrossRef]
27. Lin, L.; Jones, T.W.; Wang, J.T.W.; Cook, A.; Pham, N.D.; Duffy, N.W.; Mihaylov, B.; Grigore, M.; Anderson, K.F.; Duck, B.C.; et al. Strategically Constructed Bilayer Tin (IV) Oxide as Electron Transport Layer Boosts Performance and Reduces Hysteresis in Perovskite Solar Cells. *Small* **2020**, *16*, 1901466. [CrossRef]
28. Yi, H.; Wang, D.; Mahmud, M.A.; Haque, F.; Upama, M.B.; Xu, C.; Duan, L.; Uddin, A. Bilayer SnO_2 as Electron Transport Layer for Highly Efficient Perovskite Solar Cells. *ACS Appl. Energy Mater.* **2018**, *1*, 6027–6039. [CrossRef]
29. Wang, P.; Li, R.; Chen, B.; Hou, F.; Zhang, J.; Zhao, Y.; Zhang, X. Gradient Energy Alignment Engineering for Planar Perovskite Solar Cells with Efficiency Over 23%. *Adv. Mater.* **2020**, *32*, 1905766. [CrossRef]
30. Noh, Y.W.; Jin, I.S.; Kim, K.S.; Park, S.H.; Jung, J.W. Reduced energy loss in SnO2/ZnO bilayer electron transport layer-based perovskite solar cells for achieving high efficiencies in outdoor/indoor environments. *J. Mater. Chem. A* **2020**, *8*, 17163–17173. [CrossRef]
31. Song, J.; Zheng, E.; Wang, X.F.; Tian, W.; Miyasaka, T. Low-temperature-processed ZnO–SnO_2 nanocomposite for efficient planar perovskite solar cells. *Sol. Energy Mater. Sol. Cells* **2016**, *144*, 623–630. [CrossRef]
32. Wang, F.; Ye, Z.; Sarvari, H.; Park, S.M.; Abtahi, A.; Graham, K.; Zhao, Y.; Wang, Y.; Chen, Z.D.; Li, S. Humidity-insensitive fabrication of efficient perovskite solar cells in ambient air. *J. Power Sources* **2019**, *412*, 359–365. [CrossRef]
33. Mesquita, I.; Andrade, L.; Mendes, A. Effect of relative humidity during the preparation of perovskite solar cells: Performance and stability. *Sol. Energy* **2020**, *199*, 474–483. [CrossRef]
34. Contreras-Bernal, L.; Aranda, C.; Valles-Pelarda, M.; Ngo, T.T.; Ramos-Terrón, S.; Gallardo, J.J.; Navas, J.; Guerrero, A.; Mora-Seró, I.; Idígoras, J.; et al. Homeopathic Perovskite Solar Cells: Effect of Humidity during Fabrication on the Performance and Stability of the Device. *J. Phys. Chem. C* **2018**, *122*, 5341–5348. [CrossRef]
35. Huang, L.; Cui, X.; Liu, C.; Yang, W.; Shi, W.; Lai, J.; Wang, L. Improvement on performance of hybrid $CH_3NH_3PbI_{3-x}Cl_x$ perovskite solar cells induced sequential deposition by low pressure assisted solution processing. *Sol. Energy* **2020**, *199*, 826–831. [CrossRef]
36. La Ferrara, V.; De Maria, A.; Rametta, G.; Della Noce, M.; Mercaldo, L.V.; Borriello, C.; Bruno, A.; Veneri, P.D. ZnO nanorods/AZO photoanode for perovskite solar cells fabricated in ambient air. *Mater. Res. Express* **2017**, *4*, 085025. [CrossRef]
37. Rajamanickam, N.; Kumari, S.; Vendra, V.K.; Lavery, B.W.; Spurgeon, J.; Druffel, T.; Sunkara, M.K. Stable and durable $CH_3NH_3PbI_3$perovskite solar cells at ambient conditions. *Nanotechnology* **2016**, *27*, 235404. [CrossRef]

38. Zhou, Q.; Jin, Z.; Li, H.; Wang, J. Enhancing performance and uniformity of $CH_3NH_3PbI_{(3-x)}Cl_{(x)}$ perovskite solar cells by air-heated-oven assisted annealing under various humidities. *Sci. Rep.* **2016**, *6*, 21257. [CrossRef]
39. Nia, N.Y.; Zendehdel, M.; Cinà, L.; Matteocci, F.; Di Carlo, A. A crystal engineering approach for scalable perovskite solar cells and module fabrication: A full out of glove box procedure. *J. Mater. Chem. A* **2018**, *6*, 659–671. [CrossRef]
40. Hohenberg, P.; Kohn, W. Inhomogeneous Electron Gas. *Phys. Rev.* **1964**, *136*, B864–B871. [CrossRef]
41. Kohn, W.; Sham, L.J. Self-Consistent Equations Including Exchange and Correlation Effects. *Phys. Rev.* **1965**, *140*, A1133–A1138. [CrossRef]
42. Carnie, M.J.; Charbonneau, C.; Davies, M.L.; Troughton, J.; Watson, T.M.; Wojciechowski, K.; Snaith, H.; Worsley, D.A. A one-step low temperature processing route for organolead halide perovskite solar cells. *Chem. Commun.* **2013**, *49*, 7893–7895. [CrossRef] [PubMed]
43. Ahn, N.; Son, D.Y.; Jang, I.H.; Kang, S.M.; Choi, M.; Park, N.G. Highly Reproducible Perovskite Solar Cells with Average Efficiency of 18.3% and Best Efficiency of 19.7% Fabricated via Lewis Base Adduct of Lead(II) Iodide. *J. Am. Chem. Soc.* **2015**, *137*, 8696–8699. [CrossRef]
44. Jeon, N.J.; Noh, J.H.; Kim, Y.C.; Yang, W.S.; Ryu, S.; Seok, S.I. Solvent engineering for high-performance inorganic–organic hybrid perovskite solar cells. *Nat. Mater.* **2014**, *13*, 897–903. [CrossRef]
45. Perdew, J.P.; Burke, K.; Ernzerhof, M. Generalized Gradient Approximation Made Simple. *Phys. Rev. Lett.* **1996**, *77*, 3865–3868. [CrossRef]
46. Perdew, J.P.; Burke, K.; Ernzerhof, M. Generalized Gradient Approximation Made Simple. *Phys. Rev. Lett.* **1997**, *78*, 1396. [CrossRef]
47. Kresse, G.; Furthmüller, J. Efficient iterative schemes for ab initio total-energy calculations using a plane-wave basis set. *Phys. Rev. B* **1996**, *54*, 11169–11186. [CrossRef]
48. Kresse, G.; Furthmüller, J. Efficiency of ab-initio total energy calculations for metals and semiconductors using a plane-wave basis set. *Comput. Mater. Sci.* **1996**, *6*, 15–50. [CrossRef]
49. Kresse, G.; Hafner, J. Ab initio molecular dynamics for liquid metals. *Phys. Rev. B* **1993**, *47*, 558–561. [CrossRef] [PubMed]
50. Kresse, G.; Hafner, J. Ab initio molecular-dynamics simulation of the liquid-metal–amorphous-semiconductor transition in germanium. *Phys. Rev. B* **1994**, *49*, 14251–14269. [CrossRef] [PubMed]
51. Toroker, M.C.; Kanan, D.K.; Alidoust, N.; Isseroff, L.Y.; Liao, P.; Carter, E.A. First principles scheme to evaluate band edge positions in potential transition metal oxide photocatalysts and photoelectrodes. *Phys. Chem. Chem. Phys.* **2011**, *13*, 16644–16654. [CrossRef]
52. Pecoraro, A.; De Maria, A.; Veneri, P.D.; Pavone, M.; Muñoz-García, A.B. Interfacial electronic features in methyl-ammonium lead iodide and p-type oxide heterostructures: New insights for inverted perovskite solar cells. *Phys. Chem. Chem. Phys.* **2020**, *22*, 28401–28413. [CrossRef]
53. Blöchl, P.E. Projector augmented-wave method. *Phys. Rev. B* **1994**, *50*, 17953–17979. [CrossRef]
54. Kresse, G.; Joubert, D. From ultrasoft pseudopotentials to the projector augmented-wave method. *Phys. Rev. B* **1999**, *59*, 1758–1775. [CrossRef]
55. Grimme, S.; Antony, J.; Ehrlich, S.; Krieg, H. A consistent and accurate ab initio parametrization of density functional dispersion correction (DFT-D) for the 94 elements H-Pu. *J. Chem. Phys.* **2010**, *132*, 154104. [CrossRef]
56. Becke, A.D.; Johnson, E.R. A density-functional model of the dispersion interaction. *J. Chem. Phys.* **2005**, *123*, 154101. [CrossRef] [PubMed]
57. Grimme, S.; Ehrlich, S.; Goerigk, L. Effect of the damping function in dispersion corrected density functional theory. *J. Comput. Chem.* **2011**, *32*, 1456–1465. [CrossRef]
58. Oviedo, J.; Gillan, M.J. Energetics and structure of stoichiometric SnO_2 surfaces studied by first-principles calculations. *Surf. Sci.* **2000**, *463*, 93–101. [CrossRef]
59. Walsh, A.; Catlow, C.R.A. Structure, stability and work functions of the low index surfaces of pure indium oxide and Sn-doped indium oxide (ITO) from density functional theory. *J. Mater. Chem.* **2010**, *20*, 10438–10444. [CrossRef]
60. Dulub, O.; Boatner, L.A.; Diebold, U. STM study of the geometric and electronic structure of ZnO(0001)-Zn, $(000\bar{1})$-O, $(10\bar{1}0)$, and $(11\bar{2}0)$ surfaces. *Surf. Sci.* **2002**, *519*, 201–217. [CrossRef]
61. Fröhlich, D.; Kenklies, R.; Helbig, R. Band-Gap Assignment in SnO_2 by Two-Photon Spectroscopy. *Phys. Rev. Lett.* **1978**, *41*, 1750–1751. [CrossRef]
62. Walsh, A.; Da Silva, J.L.; Wei, S.H.; Körber, C.; Klein, A.; Piper, L.F.J.; DeMasi, A.; Smith, K.E.; Panaccione, G.; Torelli, P.; et al. Nature of the Band Gap of In_2O_3 Revealed by First-Principles Calculations and X-Ray Spectroscopy. *Phys. Rev. Lett.* **2008**, *100*, 167402. [CrossRef]
63. Srikant, V.; Clarke, D.R. On the optical band gap of zinc oxide. *J. Appl. Phys.* **1998**, *83*, 5447–5451. [CrossRef]
64. Li, Y.; Ding, B.; Chu, Q.Q.; Yang, G.J.; Wang, M.; Li, C.X.; Li, C.J. Ultra-high open-circuit voltage of perovskite solar cells induced by nucleation thermodynamics on rough substrates. *Sci. Rep.* **2017**, *7*, 46141. [CrossRef] [PubMed]
65. Kam, M.; Zhang, Q.; Zhang, D.; Fan, Z. Room-Temperature Sputtered SnO_2 as Robust Electron Transport Layer for Air-Stable and Efficient Perovskite Solar Cells on Rigid and Flexible Substrates. *Sci. Rep.* **2019**, *9*, 6963. [CrossRef]
66. Liang, Y.-C.; Chao, Y. Crystal phase content-dependent functionality of dual phase SnO_2–WO_3 nanocomposite films via cosputtering crystal growth. *RSC Adv.* **2019**, *9*, 6482–6493. [CrossRef]

67. Ozel, K.; Atilgan, A.; Koksal, N.E.; Yildiz, A. A route towards enhanced UV photo-response characteristics of SnO_2/p-Si based heterostructures by hydrothermally grown nanorods. *J. Alloy. Compd.* **2020**, *849*, 156628. [CrossRef]
68. Kirchartz, T.; Márquez, J.A.; Stolterfoht, M.; Unold, T. Photoluminescence-Based Characterization of Halide Perovskites for Photovoltaics. *Adv. Energy Mater.* **2020**, *10*, 1904134. [CrossRef]
69. Green, M.A. Accuracy of analytical expressions for solar cell fill factors. *Sol. Cells* **1982**, *7*, 337–340. [CrossRef]
70. Lou, Q.; Han, Y.; Liu, C.; Zheng, K.; Zhang, J.; Chen, X.; Du, Q.; Chen, C.; Ge, Z. π-Conjugated Small Molecules Modified SnO_2 Layer for Perovskite Solar Cells with over 23% Efficiency. *Adv. Energy Mater.* **2021**, *11*, 2101416. [CrossRef]
71. Hui, W.; Yang, Y.; Xu, Q.; Gu, H.; Feng, S.; Su, Z.; Zhang, M.; Wang, J.; Li, X.; Fang, J.; et al. Red-Carbon-Quantum-Dot-Doped SnO_2 Composite with Enhanced Electron Mobility for Efficient and Stable Perovskite Solar Cells. *Adv. Mater.* **2020**, *32*, 1906374. [CrossRef]
72. Cho, Y.; Kim, H.D.; Zheng, J.; Bing, J.; Li, Y.; Zhang, M.; Green, M.A.; Wakamiya, A.; Huang, S.; Ohkita, H.; et al. Elucidating Mechanisms behind Ambient Storage-Induced Efficiency Improvements in Perovskite Solar Cells. *ACS Energy Lett.* **2021**, *6*, 925–933. [CrossRef]
73. Moghadamzadeh, S.; Hossain, I.M.; Jakoby, M.; Nejand, B.A.; Rueda-Delgado, D.; Schwenzer, J.A.; Gharibzadeh, S.; Abzieher, T.; Khan, M.R.; Haghighirad, A.A.; et al. Spontaneous enhancement of the stable power conversion efficiency in perovskite solar cells. *J. Mater. Chem. A* **2020**, *8*, 670–682. [CrossRef]